Controlled orientation of molecular-beam-epitaxial BaTiO$_3$ on Si(001) using thickness engineering of BaTiO$_3$ and SrTiO$_3$ buffer layers

Controlled orientation of molecular-beam-epitaxial BaTiO₃ on Si(001) using thickness engineering of BaTiO₃ and SrTiO₃ buffer layers

Min-Hsiang Mark Hsu[1,2*], Dries Van Thourhout[2,3], Marianna Pantouvaki[1], Johan Meersschaut[1], Thierry Conard[1], Olivier Richard[1], Hugo Bender[1], Paola Favia[1], Maria Vila[4,5], Rosalia Cid[4,5], Juan Rubio-Zuazo[4,5], German R. Castro[4,5], Joris Van Campenhout[1], Philippe Absil[1], and Clement Merckling[1]

[1]imec, Kapeldreef 75, 3001 Leuven, Belgium
[2]Photonics Research Group, INTEC, Ghent University–imec, 9000 Gent, Belgium
[3]Center for Nano- and Biophotonics (NB-Photonics), Ghent University, 9000 Gent, Belgium
[4]SpLine CRG BM25 Beamline, European Synchrotron Radiation Facility, 38000 Grenoble, France
[5]Instituto de Ciencia de Materiales de Madrid, Consejo Superior de Investigaciones Científicas (ICMM-CSIC), 28049 Madrid, Spain

*E-mail: min.hsiang.hsu@imec.be

Monolithically integrating BaTiO₃ on silicon substrates has attracted attention because of the wide spectrum of potential novel applications ranging from electronics to photonics. For optimal device performance, it is important to control the BaTiO₃ domain orientation during thin film preparation. Here, we use molecular beam epitaxy to prepare crystalline BaTiO₃ on Si(001) substrates using a SrTiO₃ buffer layer. A systematic investigation is performed to understand how to control the BaTiO₃ domain orientation through the thickness engineering of the SrTiO₃ buffer layer and the BaTiO₃ layer itself. This provides different possibilities for obtaining a given BaTiO₃ orientation as desired for a specific device application. © 2017 The Japan Society of Applied Physics

The premier representative of the perovskite oxides, ABO_3, is $BaTiO_3$ (BTO), which has been studied for over 70 years.[1] The displacement of the Ti atom in the lattice makes BTO possess the tetragonal crystal structure, dielectric, piezoelectric, pyroelectric, and ferroelectric properties.[2–5] It is noteworthy that BTO exhibits, in several areas, characteristics that outperform any other ABO_3 material.[5–8] For this reason, the integration of crystalline BTO thin films with Si has attracted much interest for use in advanced Si-based device applications in both electronics and photonics. Recently, several groups have succeeded in this integration by inserting the $SrTiO_3$ (STO) as a buffer layer between BTO and the Si(001) substrate using molecular beam epitaxy (MBE). For example, Dubourdieu et al.[9] and Li et al.[10] demonstrated switchable ferroelectricity for nonvolatile logic applications. Additionally, in the area of silicon photonics, Xiong et al.[11] and Abel et al.[12] took advantage of the strong Pockels effect in BTO to achieve a high-speed hybrid BTO/Si optical modulator. Fundamentally, the Ti displacement in tetragonal BTO occurs along the c_{BTO} directions, allowing for six possible domain orientations in thin films: two c-oriented domains with out-of-plane dipoles and four a-oriented domains with in-plane dipoles.[5] Moreover, during the oxide synthesis, different BTO domain phases can coexist.[13] In addition, device performance is highly dependent on the BTO domain orientation and the relationship between the BTO domain orientation and the applied electric field. For example, since current ferroelectric field-effect transistor (FeFET) designs are mainly based on planar stacks of metal–ferroelectric oxide–semiconductor structures, the electric field during device operations is oriented vertically. Therefore, in practice, FeFETs require c-oriented BTO.[9,10] Also, in the performance of optical modulators, the placement of electrodes with respect to the BTO domain orientation is critical.[14,15] For this reason, it is crucial to control the BTO domain orientation during the epitaxial growth process.

In principle, the biaxial strain exerted on the BTO layer will determine its orientation: compressive and tensile strains induce c- and a-oriented BTO, respectively. However, the flexible ionic bonds in BTO and the complicated strain/relaxation mechanisms, which depend on the differential thermal expansion and lattice differences between BTO and the underlying substrate, make it very difficult to control the orientation of BTO on Si(001) substrates.[9] Several research groups have reported that using an approximately 5-nm-thick STO buffer layer, which has a small lattice constant, on Si(001) can cause thin BTO layers (thicknesses below 20 nm) to be more c-oriented.[9,16] However, for BTO layer thicknesses above 50 nm, the BTO layer will become more a-oriented owing to the tensile strain caused by the difference in thermal expansion coefficient between Si and the BTO layer.[17–19] For intermediate BTO thicknesses between 20 and 50 nm, a mixture of both a- and c-orientations has been reported. Therefore, for BTO/STO/Si(001) heterostructures, the orientation of BTO is mainly determined by a trade-off between the strains originating from the differences in the lattice constant and thermal expansion of the various layers.

In this work, we systematically study the orientation of BTO in response to this strain, as a function of the thickness of the BTO layer itself and that of the underlying STO buffer layer. We use MBE to epitaxially grow the STO buffer layer followed by the BTO layer with various thicknesses of both layers on Si(001) substrates. First, we investigate the effect of the STO thickness on the crystal structure and the interface between STO and Si(001). Then, we analyze the crystallinity and orientation of samples with different BTO thicknesses on top of a 5-nm-thick STO buffer layer. In addition, we study the orientation of BTO layers grown on STO buffer layers with various thicknesses.

All the samples are grown on 200-mm-diameter Si(001) substrates in a 200 mm Riber49 MBE production reactor. Metallic Ti is evaporated with an electron beam controlled by a feedback loop from a mass spectrometer to control the stability of the evaporation flux during growth. Both Ba and Sr atomic fluxes are obtained using standard Knudsen effusion cells and the [Sr]/[Ti] and [Ba]/[Ti] flux ratios are calibrated in situ using a quartz crystal microbalance and ex situ by Rutherford backscattering (RBS) analysis. A radio-frequency remote plasma source is used to produce atomic oxygen during growth. The detailed procedures for the surface preparation of Si(001) substrates, and the deposition and recrys-
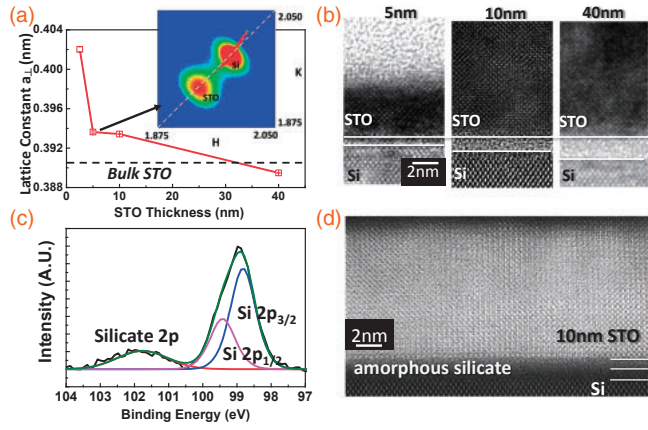
Fig. 1. (a) Lattice constant $a_\perp$ as a function of the STO layer thickness on a Si(001) substrate. The inset shows the RSM of $(220)_{Si}$ for a Si substrate and $(1.967, 1.967, 0)_{Si}$, equivalent to $(2, 0, 0)_{STO}$, for a 5-nm-thick STO layer. (b) HRTEM images of 5-, 10-, and 40-nm-thick layers of STO on Si(001). (c) Si 2p XPS scan of the 5-nm-thick STO layer on Si(001). (d) HAADF-STEM image of a 10-nm-thick STO layer on Si(001).

tallization of the first 6 monolayers (ML) (2.4 nm) of STO can be found in Ref. 9. To ensure the quality of the initial STO layer, we repeat the STO deposition and recrystallization until we reach an STO thickness of 5 nm on a Si(001) substrate. To obtain STO layers thicker than 5 nm after the second recrystallization at 550 °C, STO is allowed to continue growing under an oxygen chamber pressure of $\sim 1.2 \times 10^{-6}$ Torr. As soon as the desired STO thickness is reached, the substrate temperature is increased to 630 °C to grow the BTO layer under an oxygen chamber pressure of $\sim 1.6 \times 10^{-6}$ Torr. Then, the thicknesses of the layers are determined by spectroscopic ellipsometry (calibrated using TEM images).

Figure 1 presents the results of the crystal and interface analyses, obtained through high-resolution X-ray diffractometry (HRXRD), synchrotron radiation grazing-incidence X-ray diffractometry (SR-GIXRD),[20] transmission electron microscopy (TEM), and X-ray photoemission spectroscopy (XPS), for a series of samples with different STO thicknesses on a Si(001) substrate. To extract the STO out-of-plane lattice constants ($a_\perp$), the ω–2θ spectrum measured by HRXRD is fitted by Lorentzian functions. Then, according to $(002)_{STO}$ peak positions, the STO out-of-plane lattice constants ($a_\perp$) for layer thicknesses between 2.5 and 40 nm are extracted, as presented in Fig. 1(a). The error bars are related to the uncertainty of the peak positions during the fitting process. Bulk STO on Si with a "cube-on-cube" epitaxial relationship shows a lattice mismatch of around 28% (bulk STO: 0.3905 nm; Si: 0.5431 nm).[5] However, the introduction of 1/2 ML of Sr at the interface promotes the 45° rotation of the STO lattice with respect to the Si lattice, thereby reducing the effective lattice mismatch to 2% (Si/$\sqrt{2}$: 0.3840 nm). Therefore, Si inherently exerts compressive strain on the STO layer, prolonging the lattice in the out-of-plane direction, as measured for the 2.5-nm-thick STO sample, which has a large $a_\perp$ [Figs. 1(a)]. This also indicates that the strain in the thin STO layer does not fully relax during the recrystallization step. For STO thicknesses greater than 5 nm, the relaxation is gradual, reducing the lattice constant toward that of bulk STO. In the 5-nm-thick STO layer, $a_\perp$ is partially relaxed (larger $a_\perp$ than that of bulk STO). The in-plane relaxation for the 5-nm-thick STO layer is measured by the reciprocal space mapping

(RSM) of $(220)_{Si}$ by SR-GIXRD. The RSM results show that the STO peak tracks the relaxation line (indicated by the white dotted line) and is located at $(1.967, 1.967, 0)_{Si}$, suggesting a full relaxation in plane (in-plane lattice constant $a_\parallel = 0.3905$ nm). Therefore, the 5-nm-thick STO layer exhibits a different degree of relaxation in the in- and out-of-plane directions. As the layer thickness is increased to 40 nm, $a_\perp$ relaxes below the bulk value. Conversely, $a_\parallel$ is found to be 0.3927 nm above the bulk value, from a ω–2θ scan of $(202)_{STO}$ by HRXRD. The strain/relaxation imbalance in the STO layer is mainly caused by flexible ionic bonds. Furthermore, the mismatch of the thermal coefficient of STO ($\alpha_{STO} = 8.8 \times 10^{-6}\,°C^{-1}$ for bulk STO) and that of Si ($\alpha_{Si} = 2.6 \times 10^{-6}\,°C^{-1}$ for Si) must be considered. To quantitatively explain the thermal effect on the STO lattice, we assume that, at the recrystallization temperature of 550 °C, the STO thin film will be relaxed in the plane such that its lattice constant becomes equal to the bulk STO lattice constant ($a^{550°C STO\_Bulk}$), which is given by $a^{550°C STO\_Bulk} = a^{20°C STO\_Bulk}[1 + \alpha_{STO}(550 - 20)]$, where $a^{20°C STO\_Bulk}$, the bulk STO lattice constant at 20 °C, is equal to 0.3905 nm. Thus, the lattice constant of the STO thin film at 550 °C is 0.3923 nm. Since the STO thin film adheres onto the Si surface, during cooling to 20 °C, the contraction of the STO in-plane lattice is driven by the thermal expansion coefficient of Si,[21,22] and hence, the in-plane lattice constant of the STO thin film at 20 °C ($a_\parallel^{20°C STO\_film}$) is given by $a_\parallel^{20°C STO\_film} = a_\parallel^{550°C STO\_Bulk}[1 + \alpha_{Si}(20 - 550)]$. Therefore, $a_\parallel^{20°C STO\_film}$ becomes 0.3918 nm, which is in good agreement with our experimental value of 0.3927 nm. Furthermore, according to $(a_\perp^{20°C STO\_film} - a^{20°C STO\_Bulk}) = -2 \cdot (C_{12}/C_{11}) \cdot (a_\parallel^{20°C STO\_film} - a^{20°C STO\_Bulk})$, where $a_\perp^{20°C STO\_film}$ is the out-of-plane lattice constant of the STO thin film at 20 °C and $C_{12}/C_{11} = 0.3228$, we find $a_\perp^{20°C STO\_film} = 0.3897$ nm, which is consistent with our measured value of 0.3895 nm. To summarize, the strain of the 2.5-nm-thick STO layer is mainly governed by compressive strain from Si leading to a large $a_\perp$. However, the strain/relaxation mechanism for the thicker STO layer is determined more by thermal expansion, which leads to tensile strain, thereby reducing $a_\perp$.

Figure 1(b) shows cross-sectional high-resolution TEM (HR-TEM) images along the $[110]_{Si}$ zone axis for 5-, 10-, and 40-nm-thick STO layers on Si. The relative orientations of the structures are $[100]_{STO} \parallel [110]_{Si}$ along the zone axis and $[001]_{STO} \parallel [001]_{Si}$ in the vertical direction. Because of the thermodynamic instability of the system,[8] an amorphous interfacial layer (IL) is formed between the STO layer and the Si(001) substrate. However, for the 5-nm-thick STO layer, this interfacial layer is barely observable. Hence, we conduct XPS on 5-nm-thick STO/Si heterostructures to analyze the interface further, as shown in Fig. 1(c). The silicate peak near the Si 2p core level can be observed near ~ 102 eV. By fitting its peak area, the thickness of the IL is determined to be around 0.7 nm. The combination of TEM and XPS characterization allows the thickness of each amorphous layer to be extracted and compared [as shown in Fig. 1(b)], showing that the IL grows with STO thickness. From the high-angle annular dark-field scanning TEM (HAADF-STEM) image shown in Fig. 1(d), we can conclude that this IL is actually composed of two layers. Since the contrast in HAADF-STEM images is proportional to the square of the atomic number (Z^2), the brightness of the double layers at the
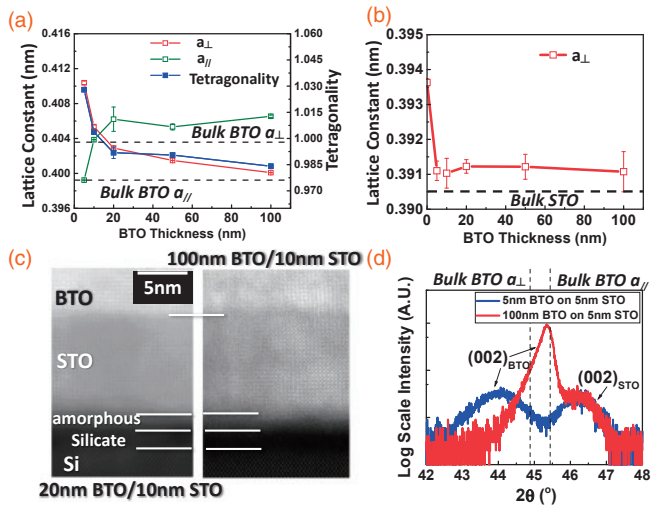
Fig. 2. (a) Lattice constants, $a_\perp$ and $a_\parallel$, and tetragonality of BTO of different layer thicknesses on a 5-nm-thick STO layer. (b) $a_\perp$ of STO for samples with different BTO layer thicknesses on a 5-nm-thick STO layer. (c) HAADF-STEM images of 20- and 100-nm-thick BTO layers on a 10-nm-thick STO buffer layer. (d) ω–2θ scans of $(002)_{BTO/STO}$ for 5- and 100-nm-thick BTO layers on a 5-nm-thick STO layer.

Fig. 3. (a) Ba χ_{min} for RBS channeling and FWHM of the $(002)_{BTO}$ rocking curve, $\Delta\omega$, for various BTO layer thicknesses on 5-nm-thick STO layers. (b) Series of RHEED images showing different BTO layer thicknesses on a 5-nm-thick STO buffer layer.

interface indicates that they have different compositions. Electron dispersion spectroscopy (EDS) measurements show that the whole IL is composed of a silicate compound with a graded distribution of Si, O, Sr, and Ti, which is the result of diffusion processes during the STO recrystallization step at high temperatures. The top layer contains more Sr and Ti, while the bottom layer is more SiO_x-rich.

Furthermore, we also study the effect of the BTO thickness on both the BTO and STO crystal structures and investigate the interface stability. BTO layers with thicknesses ranging from 5 to 100 nm are grown on Si(001) with a 5-nm-thick STO buffer layer. For BTO thicknesses below 20 nm, the BTO in-plane lattice constant $a_\parallel$ is evaluated using a scan from the origin to $(220)_{Si}$ in reciprocal space by SR-GIXRD. The thicker layers are evaluated using ω–2θ scans of $(202)_{BTO}$ Bragg reflections by HRXRD. The values of $a_\perp$ for all the BTO layer samples are determined by studying $(002)_{BTO}$ by HRXRD. It should be noted that, for a-oriented BTO, the four equivalent domain orientations in the plane should result in double peaks corresponding to $(202)_{BTO}$ and $(220)_{BTO}$ related to the distinct in-plane lattice constants, c and a. However, it is challenging to resolve the double peaks in our HRXRD setup due to the small difference in lattice constant. For this reason, the in-plane lattice constant ($a_\parallel$) for BTO used in this work is an average value. Figure 2(a) presents the evolution of the BTO lattice constant, including $a_\perp$, $a_\parallel$, and the tetragonality ($a_\perp/a_\parallel$), as a function of the thickness of BTO grown on a 5-nm-thick STO buffer layer on Si(001). We clearly observe that, with increasing BTO thickness, the out-of-plane lattice $a_\perp$ decreases, while the in-plane lattice constant $a_\parallel$ increases. The evolution of the tetragonality suggests that BTO flips from the c-orientation to the a-orientation as the thickness increases. When the thickness of the BTO layer is below 20 nm, the compressive strain originating from the larger in-plane BTO lattice constant (bulk c-oriented BTO: $a_\parallel = 0.3992$ nm vs bulk STO $a_\parallel = 0.3905$ nm) is dominant. This causes BTO to become more c-oriented. However, for BTO thicknesses greater than 20 nm, the strain caused by the
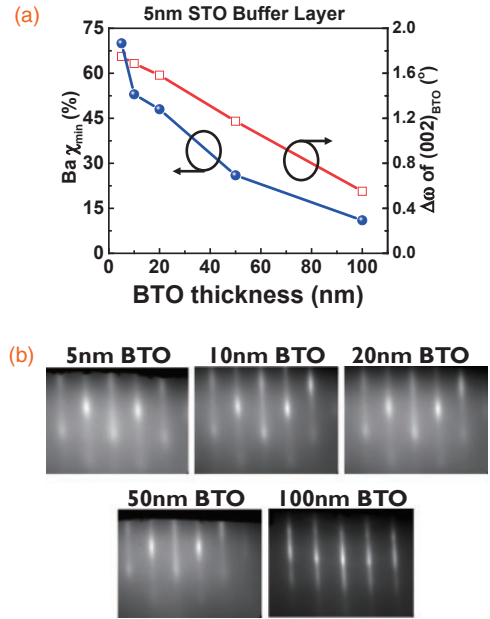
thermal expansion starts to play a role. Since the BTO spaced by the 5 nm STO buffer is close to the Si surface, during cooling after growth, the thermal expansion of Si drives the contraction of the BTO in-plane lattice. As indicated by the huge difference in thermal expansion coefficient between BTO ($\alpha_{BTO} = 11 \times 10^{-6}$ K^{-1} for bulk BTO) and Si, the tensile strain causes the BTO orientation to change from out-of-plane to in-plane. It should also be noted that the volume of a BTO unit cell on 5 nm STO is larger than the bulk BTO unit cell volume, indicating that some point defects are generated during growth. Furthermore, the change in $a_\perp$ for the 5-nm-thick STO film covered with BTO layers of various thicknesses is shown in Fig. 2(b). When a 5-nm-thick BTO layer is grown on the 5-nm-thick STO layer, the $a_\perp$ of STO is relaxed and remains low for BTO layer thicknesses between 20 and 100 nm. The same can be observed in the HAADF-STEM image in Fig. 2(c). BTO layers 20 and 100 nm thick have a similarly thick amorphous silicate region at the interface between the 10-nm-thick STO layer and the Si substrate. Figure 2(d) presents the ω–2θ scans of $(002)_{BTO/STO}$ obtained by HRXRD for the thinnest (5 nm) and thickest (100 nm) BTO layers on the 5-nm-thick STO buffer layer. When the BTO thickness increases, the width of the $(002)_{BTO}$ peak decreases, indicating the increase in crystallite size within the BTO layer. According to the Scherrer equation, the evaluated crystallite size for the 100 nm BTO layer is around 25 nm.

In addition, we investigate the dependence of the crystallinity of the BTO layers on their thickness. First, RBS channeling is performed to quantitatively analyze the BTO crystallinity. In principle, the higher the layer quality, the more alpha particles can be channeled without being scattered. Therefore, higher quality layers will have a lower minimum yield (χ_{min}), defined by the signal ratio of the channeled and random particles. In Fig. 3(a), Ba χ_{min} reveals that the BTO quality improves as the BTO thickness increases. Figure 3(a) also shows the full width at half maximum (FWHM) of the
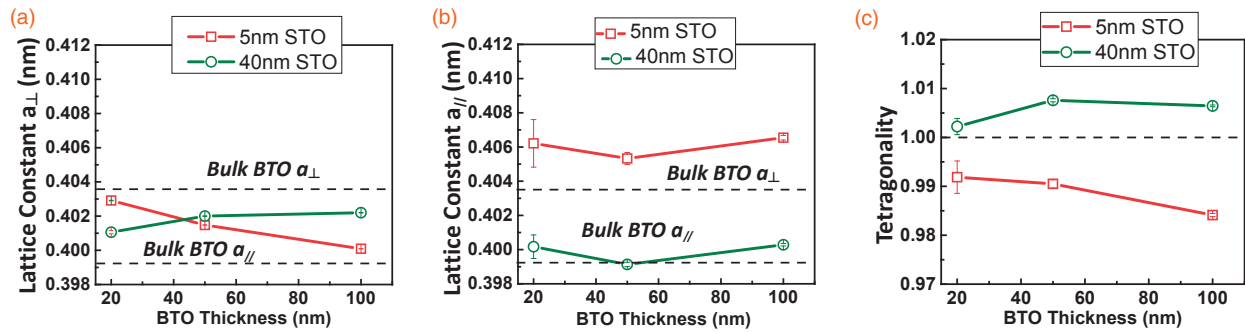
Fig. 4. (a) $a_\perp$, (b) $a_\parallel$, and (c) tetragonality of BTO films of different thicknesses on 5- and 40-nm-thick STO buffer layers.

(002)$_{BTO}$ rocking curve ($\Delta\omega$) acquired using HRXRD. The evolution of the FWHM shows the same trend as that of Ba χ_{min}: the FWHM decreases as the BTO thickness increases. Additionally, the RHEED streak line patterns in Fig. 3(b) show that thicker BTO layers have higher intensities, sharpness, and contrast against the background. Thus, the data obtained from RBS channeling, HRXRD, and RHEED all confirm that the quality of the BTO layer improves as its thickness increases.

In the previous section, we note that the strain in the 5- and 10-nm-thick BTO layers is dominated by lattice effects of the underlying stacks (STO and Si), which exert compressive strain on the BTO layer. However, for BTO layers thicker than 10 nm, the thermal expansion effect becomes pronounced. To understand the BTO relaxation behavior better, we prepare a series of heterostructures with BTO layers of several thicknesses (20, 40, and 100 nm) grown on STO buffer layers with different thicknesses (5 and 40 nm). In Fig. 4(a), the $a_\perp$ values of BTO on 5 nm STO layers decrease until they are the same as the bulk BTO $a_\parallel$ value when the BTO layer thickness increases. We also note that the $a_\perp$ of BTO with a 40-nm-thick STO layer is constant regardless of the BTO layer thickness. Furthermore, as can be observed in Fig. 4(b), with a thicker STO buffer layer, the $a_\parallel$ of a 20- to 100-nm-thick BTO layer is smaller and closer to that of bulk BTO. Thus, the tetragonality in Fig. 4(c) shows that BTO samples on 5-nm-thick STO layers are a-oriented, while those grown on 40-nm-thick STO layers are c-oriented. As mentioned previously, the thick BTO layers on the 5 nm STO buffer inherently tend to show a-orientation owing to the tensile strain originating from the difference between the thermal expansion coefficient of BTO and that of Si. Nevertheless, when using a 40-nm-thick STO buffer layer as a spacer between BTO and Si, this effect becomes less important. As a consequence, c-oriented BTO layers can be obtained.

1) E. Heymann and H. Bloom, Nature **156**, 479 (1945).
2) L. Mazet, R. Bachelet, L. Louahadj, D. Albertini, B. Gautier, R. Cours, S. Schamm-Chardon, G. Saint-Girons, and C. Dubourdieu, J. Appl. Phys. **116**, 214102 (2014).
3) L. Mazet, S. M. Yang, S. V. Kalinin, S. Schamm-Chardon, and C. Dubourdieu, Sci. Technol. Adv. Mater. **16**, 036005 (2015).
4) R. Guo, Z. Wang, S. Zeng, K. Han, L. Huang, D. G. Schlom, T. Venkatesan, Ariando, and J. Chen, Sci. Rep. **5**, 12576 (2015).
5) A. A. Demkov and A. B. Posadas, *Integration of Functional Oxides with Semiconductors* (Springer, New York, 2014).
6) J. W. Reiner, A. M. Kolpak, Y. Segal, K. F. Garrity, S. Ismail-Beigi, C. H. Ahn, and F. J. Walker, Adv. Mater. **22**, 2919 (2010).
7) S. H. Baek and C. B. Eom, Acta Mater. **61**, 2734 (2013).
8) D. G. Schlom, L. Q. Chen, X. Pan, A. Schmehl, and M. A. Zurbuchen, J. Am. Ceram. Soc. **91**, 2429 (2008).
9) C. Dubourdieu, J. Bruley, T. M. Arruda, A. Posadas, J. Jordan-Sweet, M. M. Frank, E. Cartier, D. J. Frank, S. V. Kalinin, A. A. Demkov, and V. Narayanan, Nat. Nanotechnol. **8**, 748 (2013).
10) Z. Li, X. Guo, H. B. Lu, Z. Zhang, D. Song, S. Cheng, M. Bosman, J. Zhu, Z. Dong, and W. Zhu, Adv. Mater. **26**, 7185 (2014).
11) C. Xiong, W. H. Pernice, J. H. Ngai, J. W. Reiner, D. Kumah, F. J. Walker, C. H. Ahn, and H. X. Tang, Nano Lett. **14**, 1419 (2014).
12) S. Abel, T. Stoferle, C. Marchiori, D. Caimi, L. Czornomaz, M. Stuckelberger, M. Sousa, B. J. Offrein, and J. Fompeyrine, J. Lightwave Technol. **34**, 1688 (2016).
13) C. Merckling, G. Saint-Girons, C. Botella, G. Hollinger, M. Heyns, J. Dekoster, and M. Caymax, Appl. Phys. Lett. **98**, 092901 (2011).
14) P. Castera, D. Tulli, A. M. Gutierrez, and P. Sanchis, Opt. Express **23**, 15332 (2015).
15) A. Petraru, J. Schubert, M. Schmid, and C. Buchal, Appl. Phys. Lett. **81**, 1375 (2002).
16) K. J. Kormondy, S. Abel, F. Fallegger, Y. Popoff, P. Ponath, A. B. Posadas, M. Sousa, D. Caimi, H. Siegwart, E. Uccelli, L. Czornomaz, C. Marchiori, J. Fompeyrine, and A. A. Demkov, Microelectron. Eng. **147**, 215 (2015).
17) S. Abel, M. Sousa, C. Rossel, D. Caimi, M. D. Rossell, R. Erni, J. Fompeyrine, and C. Marchiori, Nanotechnology **24**, 285701 (2013).
18) D. M. Kim, C. B. Eom, V. Nagarajan, J. Ouyang, R. Ramesh, V. Vaithyanathan, and D. G. Schlom, Appl. Phys. Lett. **88**, 142904 (2006).
19) M. H. M. Hsu, C. Merckling, S. El Kazzi, M. Pantouvaki, O. Richard, H. Bender, J. Meersschaut, J. V. Campenhout, P. Absil, and D. V. Thourhout, J. Appl. Phys. **120**, 225114 (2016).
20) J. Rubio-Zuazo, P. Ferrer, A. Lopez, A. Gutierrez-Leon, I. da Silva, and G. R. Castro, Nucl. Instrum. Methods Phys. Res., Sect. A **716**, 23 (2013).
21) G. Delhaye, C. Merckling, M. El-Kazzi, G. Saint-Girons, M. Gendry, Y. Robach, G. Hollinger, L. Largeau, and G. Patriarche, J. Appl. Phys. **100**, 124109 (2006).
22) N. Lucas, H. Zabel, H. Morkoc, and H. Unlu, Appl. Phys. Lett. **52**, 2117 (1988).